



Harmonic response computation of poroelastic multilayered structures using ZPST shell elements



Jean-Daniel Chazot^{a,*}, Benoit Nennig^b, Emmanuel Perrey-Debain^a

^a Université de Technologie de Compiègne, Laboratoire Roberval UMR 7337, BP 20529, 60205 Compiègne cedex, France

^b Laboratoire d'Ingénierie des Systèmes Mécaniques et des Matériaux (LISMM), SUPMECA, 3 rue Fernand Hainaut, 93407 Saint-Ouen, France

ARTICLE INFO

Article history:

Received 8 August 2012

Accepted 18 February 2013

Available online 17 April 2013

Keywords:

Shell element

Multilayer

ZPST

Zigzag

Porous

Poroelastic

ABSTRACT

This paper uses a multilayered shell element to compute the dynamic response of multilayered poroelastic structures such as car instrument panels, car floors, or car roofs. It is based on the P-order Shear deformation Theory with an added Zigzag function (ZPST). Biot's theory is used to describe the poroelastic layer and standard couplings are realized between elastic and poroelastic layers. A method based on Padé approximants is also used in order to reduce the computation time. This acceleration technique enables to achieve fast frequency sweep computations compared to a standard direct method. Finally, numerical validations on plates and curved geometries are presented.

© 2013 Elsevier Ltd. All rights reserved.

1. Introduction

Porous materials are used in a wide range of industrial applications for which noise control problems must be tackled. In the transport industry, such as automotive and aeronautics for instance, these materials are very efficient to reduce the transmission of sound from one area to another. To predict their behavior, 3D finite element models (FEM) [1,2] based on Biot's theory [3–5] are employed with several parameters related to the microstructure of the porous material [6]. The homogenized behavior of the fluid and solid phases is then described with all the inertial and elastic interactions. Structural, viscous and thermal dissipations are also taken into account. Because these three dimensional numerical models can become very large (from a computational point view), simplified models such as the Limp model [7] or the Fluid–Fluid model [8] can sometimes be used to reduce the computational effort. However, these are only valid under some assumptions which limit their use for a specific range of materials and configurations.

In practice, foam and fibrous materials are often bonded to thin structures. In simple academic cases, analytical formulations are available to model such multilayered structures [9]. However, for more complex geometries and boundary conditions that are often encountered in industrial configurations 3D FE simulations are still needed. Each layer is then modeled separately with 3D elements.

Here again, the method turns out to be cumbersome and time-consuming both in terms of data preparation and computation.

On the other hand, multilayered shell elements enable to reduce these costs when dealing with elastic or viscoelastic multilayered materials. Among the possible shell models, one can distinguish three different kinds. The simplest models are based on the First-order Shear Deformation Theory (FSDT) [10,11] with linear displacements across the thickness of each layer. Then, in the P-order Shear Deformation Theory (PSDT), a p -order polynomial is used to describe the displacements across the thickness [12–14]. The displacement is however not always a smooth function as its first derivative is generally discontinuous at the layers interface. This makes the displacements difficult to describe accurately with polynomial shape functions. This phenomena is particularly visible when elastic properties are very different in each layer. A high order approximation is then necessary to model the in-plane and transverse displacements as shown by Cugnoni et al. in the PSDT model [12,13]. A zigzag function can also be added to tackle this limitation [15–19] and to reduce the approximation order that is necessary with the previous PSDT model. The resulting ZPST model developed by Sulmoni et al. [18] was successfully applied by the present authors to the modeling of viscoelastic layers [20].

As a natural extension, this paper presents a shell element adapted to multilayered structures with poroelastic materials. It is based on the ZPST model. A specific resolution method is also presented. Here, due to the frequency dependency of the mass and stiffness matrices, the classical modal method cannot be

* Corresponding author. Tel.: +33 3 44 23 45 38.

E-mail address: jean-daniel.chazot@utc.fr (J.-D. Chazot).

employed to compute the Frequency Response Function (FRF). Direct frequency response methods have to be used instead. However, when the model size becomes important due to the cumulative effect of high order approximations, large refined meshes and a dense grid of frequency points, the computational cost may be prohibitive. Specific numerical methods, based for example on the extension of complex modes [21] or on a substructuring approach [22,23], are then useful to circumvent this difficulty. Methods based on Padé approximants [24–27] can also be used in a similar way to limit the computational time. The main advantage of these methods stems from their ability to overcome the convergence problems around resonances that are usually observed with standard approximation methods such as the power series expansion. This is a key point for resonant problems encountered in acoustics and vibrations. Recently, a new approach for Padé approximants has been presented by Avery et al. [24]. Finally, the authors have shown in Ref. [20] that the Padé approximants technique was well suited for vibroacoustics problems including viscoelastic materials.

$$\Delta p_f + \omega^2 \frac{\rho_{22}}{R} p_f = \omega^2 \tilde{\gamma} \frac{\rho_{22}}{\phi^2} \nabla \cdot \mathbf{u}, \quad (3b)$$

where $\boldsymbol{\sigma}^s$ is the solid stress tensor in vacuo, ϕ is the porosity, R is related to the dynamic fluid compressibility K_f with $R = \phi K_f$, $\tilde{\rho}$ is the effective density such as $\tilde{\rho} = \rho_{11} - \rho_{12}^2/\rho_{22}$, and $\tilde{\gamma}$ is given by $\tilde{\gamma} = \phi(\rho_{12}/\rho_{22} - (1 - \phi)/\phi)$. The inertial coupling coefficients ρ_{11} , ρ_{22} , and ρ_{12} , and the frequency-dependent Johnson–Allard's expressions of the fluid density ρ_f and the dynamic fluid compressibility K_f are reminded in Appendix A. Finally, the solid stress tensor in vacuo is related to the solid strain $\boldsymbol{\varepsilon}^s$ as

$$\boldsymbol{\sigma}^s = (A - Q^2/R)\nabla \cdot \mathbf{u} \mathbf{I} + 2N\boldsymbol{\varepsilon}^s. \quad (4)$$

Elastic coefficients A , Q and R are also reminded in Appendix A, and \mathbf{I} is the identity matrix.

The associated (\mathbf{u}, p_f) weak integral formulation detailed in Refs. [2,9] is used here for the poroelastic layers:

$$\underbrace{\int_{V_p} (\delta \boldsymbol{\varepsilon}^s : \boldsymbol{\sigma}^s - \tilde{\rho} \omega^2 \delta \mathbf{u} \cdot \mathbf{u}) dV}_{\text{Solid phase}} + \underbrace{\int_{V_p} \left(\frac{\phi^2}{\omega^2 \rho_{22}} \nabla p_f \cdot \nabla \delta p_f - \frac{\phi^2}{R} p_f \delta p_f \right) dV}_{\text{Fluid phase}} - \underbrace{\int_{V_p} \left[\tilde{\gamma} + \phi \left(1 + \frac{Q}{R} \right) \right] \delta (\nabla p_f \cdot \mathbf{u}) dV - \int_{V_p} \left[\phi \left(1 + \frac{Q}{R} \right) \right] \delta (p_f \cdot \nabla \mathbf{u}) dV}_{\text{Coupling between the two phases}} - \underbrace{\int_{S_p} (\boldsymbol{\sigma}^t \mathbf{n}) \cdot \delta \mathbf{u} dS - \int_{S_p} \phi (\mathbf{U} \cdot \mathbf{n} - \mathbf{u} \cdot \mathbf{n}) \delta p_f dS}_{\text{Boundary terms}} = 0, \quad (5)$$

The paper is organized as follows: after reminding in Section 2 the classical variational formulations associated with the elastic and the poroelastic wave equations, the finite element discretization of the multilayered structure using ZPST multilayered shell elements is presented in Section 3. The Padé reconstruction method is explained in Section 4 and some results including validations with conventional 3D models are shown in Section 5.

2. Variational formulation

2.1. Elastic and viscoelastic layers

For elastic or viscoelastic layers, the forced harmonic vibration problem is described by the classical variational formulation (see Ref. [20]):

$$\int_{V_e} (\delta \boldsymbol{\varepsilon} : \boldsymbol{\sigma} - \rho \omega^2 \delta \mathbf{u} \cdot \mathbf{u}) dV - \int_{S_e} (\boldsymbol{\sigma} \mathbf{n}) \cdot \delta \mathbf{u} dS = 0, \quad (1)$$

where $\boldsymbol{\varepsilon}$ and $\boldsymbol{\sigma}$ are the strain and stress tensors, \mathbf{u} the solid displacement, ρ the density, and \mathbf{n} the unit outward normal. When the harmonic excitation is in the form of a known force \mathbf{F}_e applied over a surface S_e , the boundary term writes:

$$\int_{S_e} (\boldsymbol{\sigma} \mathbf{n}) \cdot \delta \mathbf{u} dS = \int_{S_e} \mathbf{F}_e \cdot \delta \mathbf{u} dS. \quad (2)$$

2.2. Poroelastic layers

Poroelastic materials are defined by Biot [3–5] as materials with a fluid and a solid phase. Elastic, inertial, viscous and thermal interactions between the two phases are hence taken into account. For time harmonic problems ($e^{-j\omega t}$), the Biot poroelasticity equations are written in a reduced form using only the solid displacement and fluid pressure (\mathbf{u}, p_f) variables (see Ref. [2]):

$$\nabla \cdot \boldsymbol{\sigma}^s + \omega^2 \tilde{\rho} \mathbf{u} = -\tilde{\gamma} \nabla p_f, \quad (3a)$$

with $\boldsymbol{\sigma}^t$ the total stress tensor such as $\boldsymbol{\sigma}^t = \boldsymbol{\sigma}^s + \boldsymbol{\sigma}^f$ and \mathbf{U} the fluid phase displacement. The fluid stress tensor $\boldsymbol{\sigma}^f$ is here directly related to the fluid pressure p_f with $\boldsymbol{\sigma}^f = -\phi p_f \mathbf{I}$, and the fluid displacement \mathbf{U} does not need to be stated explicitly as it will be removed after applying the boundary conditions.

In this formulation, one can distinguish the terms related to the solid and the fluid phases, the coupling terms between the two phases, and the boundary terms at the porous interface S_p .

2.3. Coupling conditions

At the interface between an elastic layer and a poroelastic layer the continuity of the total stresses and the continuity of the solid displacements apply. Moreover the solid and fluid normal displacements of the porous material are also constrained by the solid displacement of the elastic layer. The coupling conditions between an elastic layer 1 and a poroelastic layer 2 writes:

$$\boldsymbol{\sigma}_1 \mathbf{n} = \boldsymbol{\sigma}_2^t \mathbf{n}, \quad (6)$$

$$\mathbf{u}_1 = \mathbf{u}_2, \quad (7)$$

$$\mathbf{U}_2 \cdot \mathbf{n} - \mathbf{u}_2 \cdot \mathbf{n} = 0. \quad (8)$$

This coupling is therefore very simple to implement since all the boundary terms vanish at each porous-elastic interface.

3. Finite element formulation

The finite element ZPST used in this paper is depicted in Fig. 1. The formulation presented in details by Sulmoni et al. in Ref. [18] and applied to viscoelastic materials in Ref. [20] is reminded here briefly.

3.1. Solid displacement approximation

The solid displacement approximation in all the layers is shown in Fig. 2 with the p -order approximation and the zigzag function.

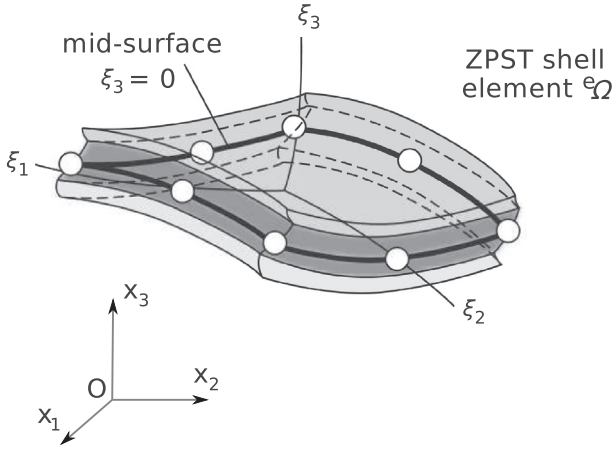


Fig. 1. ZPST shell element.

The zigzag function is added in order to enhance the convergence of the solution at the interfaces. The same approximation is used for the in-plane displacements along ξ_1 and ξ_2 , and for the normal displacement along ξ_3 .

The displacement vector ${}^e\mathbf{u}$ over the element e is described using a p -order polynomial and a first-order zigzag function as:

$${}^e\mathbf{u}(\xi) = \sum_{i=1}^n H_i(\xi_1, \xi_2) \left[{}^e\mathbf{q}_{u_i}^{(0)} + \xi_3^e \mathbf{q}_{u_i}^{(1)} + \frac{\xi_3^{2e} \mathbf{q}_{u_i}^{(2)}}{2!} + \dots + \frac{\xi_3^{pe} \mathbf{q}_{u_i}^{(p)}}{p!} + (-1)^K \zeta^e \mathbf{q}_{u_i}^{(Z)} \right], \quad (9)$$

where $\xi = \{\xi_1, \xi_2, \xi_3\}$ is the local coordinates vector, H_i is the i th shape function of the n -nodes quadratic shell element, $\mathbf{q}_{u_i}^{(j)}$ is the vector with the displacements' degrees of freedom of node i at the order j , $\mathbf{q}_{u_i}^{(Z)}$ is

$$\mathbf{H}_{u_i} = \begin{bmatrix} H_i & 0 & 0 & 0 & \xi_3 H_i & 0 & 0 & 0 & (-1)^K \zeta H_i & 0 & 0 & 0 & \dots & \xi_3^p H_i / p! & 0 & 0 & 0 \\ 0 & H_i & 0 & 0 & 0 & \xi_3 H_i & 0 & 0 & 0 & (-1)^K \zeta H_i & 0 & 0 & \dots & 0 & \xi_3^p H_i / p! & 0 & 0 \\ 0 & 0 & H_i & 0 & 0 & 0 & \xi_3 H_i & 0 & 0 & 0 & (-1)^K \zeta H_i & 0 & \dots & 0 & 0 & \xi_3^p H_i / p! & 0 \end{bmatrix}$$

and

$$\mathbf{H}_p = [0 \ 0 \ 0 \ H_i \ 0 \ 0 \ 0 \ \xi_3 H_i \ 0 \ 0 \ 0 \ (-1)^K \zeta H_i \ \dots \ 0 \ 0 \ 0 \ \xi_3^p H_i / p!].$$

the vector with the displacements' degrees of freedom of node i corresponding to the zigzag function, K is the layer index and ζ is the transverse layer coordinate normalized between -1 and $+1$. Intro-

ducing t_k the thickness of the k th layer and t_t the total thickness of the multilayer, the relation between the local through-the-thickness coordinate ξ_3 and the transverse layer coordinate ζ writes:

$$\xi_3 = -1 + 2 \sum_{k=1}^{K-1} \frac{t_k}{t_t} + (1 + \zeta) \frac{t_K}{t_t}. \quad (10)$$

3.2. Fluid pressure approximation in the porous layers

For the sake of simplicity, the same approximation is used for the fluid pressure in the porous domain:

$${}^e p_f(\xi) = \sum_{i=1}^n H_i(\xi_1, \xi_2) \left[{}^e q_{p_i}^{(0)} + \xi_3^e q_{p_i}^{(1)} + \frac{\xi_3^{2e} q_{p_i}^{(2)}}{2!} + \dots + \frac{\xi_3^{pe} q_{p_i}^{(p)}}{p!} + (-1)^K \zeta^e q_{p_i}^{(Z)} \right], \quad (11)$$

where $q_{p_i}^{(j)}$ is the pressure's degree of freedom of node i at the order j , and $q_{p_i}^{(Z)}$ is the pressure's degree of freedom of node i corresponding to the zigzag function. This approximation is global over the whole thickness of the multilayered structure although it is only active for poroelastic layers. We may observe that multilayers made of only one poroelastic layer do not need the zigzag function for the pressure as the polynomial approximation is sufficient. The zigzag function is removed in this case in order to avoid redundancy.

3.3. Global approximation

The displacements' and pressure's degrees of freedom \mathbf{q}_u and \mathbf{q}_p are collected in a single vector \mathbf{q} . Eqs. (9) and (11) are expressed in a reduced matrix form:

$${}^e\mathbf{u}(\xi) = \mathbf{H}_u(\xi) {}^e\mathbf{q} \quad \text{and} \quad {}^e p_f(\xi) = \mathbf{H}_p(\xi) {}^e\mathbf{q}, \quad (12)$$

where $\mathbf{H}_u(\xi)$ and $\mathbf{H}_p(\xi)$ are the displacement and pressure interpolation matrices over the n -nodes element, $\mathbf{H}_u(\xi) = [\mathbf{H}_{u_1}, \mathbf{H}_{u_2}, \dots,$

$$\mathbf{H}_p(\xi) = [\mathbf{H}_{p_1}, \mathbf{H}_{p_2}, \dots, \mathbf{H}_{p_n}]$$

respectively, with the total number of dofs by node is thus equal to $\text{NDOF}_n = 4(p+2)$, and $\text{NDOF}_n = 4(p+2) - 1$ when the zigzag function is

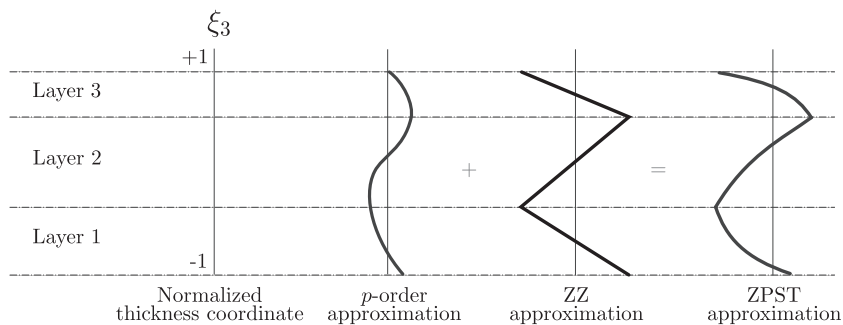


Fig. 2. ZPST displacement approximation.

removed for the pressure approximation. For a quadratic quadrangle Q8 the number of dofs is therefore equal to $\text{NDOF}_e = 32(p + 2)$ and $\text{NDOF}_e = 32(p + 2) - 8$ without the zigzag function.

3.4. Finite element discretization

The finite element discretization of the variational formulations (1) and (5) is introduced and matrices \mathbf{H}_u and \mathbf{H}_p are used to approximate the displacements and the pressure over each element. In the elastic layers, the following elementary mass, stiffness, and force matrices are obtained:

$$\begin{aligned} {}^e\mathbf{M}_e &= \int_{eV_e} \rho \mathbf{H}_u^t \mathbf{H}_u \, dV, & {}^e\mathbf{K}_e &= \int_{eV_e} {}^e\mathbf{B}^t \mathbf{C}^e \mathbf{B} \, dV, \\ {}^e\mathbf{F}_e &= \int_{eV_e} \mathbf{H}_u^t \mathbf{F}_e \, dV, \end{aligned} \quad (13)$$

where ${}^e\mathbf{B}$ refers to the strain–displacement matrix, while ${}^e\mathbf{C}$ refers to the strain–stress matrix. In the poroelastic layers, elementary mass and stiffness matrices write:

$${}^e\mathbf{M}_{pe} = \tilde{\rho} \underbrace{\int_{eV_p} \mathbf{H}_u^t \mathbf{H}_u \, dV}_{{}^e\mathbf{M}_1} \quad (14)$$

$$\begin{aligned} {}^e\mathbf{K}_{pe} &= \int_{eV_p} \left({}^e\mathbf{B}^t \mathbf{C}^e \mathbf{B} - \phi \left(1 + \frac{Q}{R} \right) (\mathbf{V}\mathbf{H}_p^t \mathbf{H}_u + \mathbf{H}_u^t \mathbf{V}\mathbf{H}_p + \mathbf{H}_p^t \mathbf{V}\mathbf{H}_u + \mathbf{V}\mathbf{H}_u^t \mathbf{H}_p) \right) dV \\ &\quad + \frac{\phi^2}{\omega^2 \rho_{22}} \underbrace{\int_{eV_p} \mathbf{V}\mathbf{H}_p^t \mathbf{V}\mathbf{H}_p \, dV}_{{}^e\mathbf{K}_1} - \frac{\phi^2}{R} \underbrace{\int_{eV_p} \mathbf{H}_p^t \mathbf{H}_p \, dV}_{{}^e\mathbf{K}_2} \\ &\quad - \tilde{\gamma} \underbrace{\int_{eV_p} (\mathbf{V}\mathbf{H}_p^t \mathbf{H}_u + \mathbf{H}_u^t \mathbf{V}\mathbf{H}_p) \, dV}_{{}^e\mathbf{K}_3} \end{aligned} \quad (15)$$

where ${}^e\mathbf{B}$ and ${}^e\mathbf{C}$ refer also to the strain–displacement and strain–stress matrices of the solid phase, respectively, and \mathbf{V} stands for the differential operator in the global coordinates. Note the frequency-dependent parameters have been isolated in these equations and resulting matrices ${}^e\mathbf{M}_1$, ${}^e\mathbf{K}_0$, ${}^e\mathbf{K}_1$, ${}^e\mathbf{K}_2$, and ${}^e\mathbf{K}_3$ do not depend on frequency.

The elementary mass and stiffness matrices are obtained by summing the elastic and poroelastic elementary matrices. Given that each element is made up of several layers with different properties, it is necessary to integrate these matrices separately over each layer. Finally, the curved shell element is obtained from a master element. The integration over the curved element can be found in Ref. [18] with the details of the Jacobian of the geometric transformation. A numerical integration using Gauss–Legendre quadratures is used to calculate the elementary matrices.

The final global matrix is created by the assembly of elementary matrices:

$$(\mathbf{K}(\omega) - \omega^2 \mathbf{M}(\omega)) \mathbf{U} = \mathbf{F}, \quad (16)$$

where $\mathbf{K}(\omega)$ and $\mathbf{M}(\omega)$ are the global stiffness and mass matrices, \mathbf{U} is the generalized nodal displacement with all the degrees of freedom and \mathbf{F} is the generalized nodal excitation. In this equation, $\mathbf{K}(\omega)$ and $\mathbf{M}(\omega)$ are symmetric. The problem can also be written in the compact form

$$\mathbf{Z}(\omega) \mathbf{U} = \mathbf{F}(\omega), \quad (17)$$

by introducing a global impedance matrix $\mathbf{Z}(\omega)$ defined as:

$$\mathbf{Z}(\omega) = \mathbf{K}_e - \omega^2 \mathbf{M}_e + \mathbf{K}_0 + \frac{\phi^2}{\omega^2 \rho_{22}} \mathbf{K}_1 - \frac{\phi^2}{R} \mathbf{K}_2 - \tilde{\gamma} \mathbf{K}_3 - \tilde{\rho} \omega^2 \mathbf{M}_0, \quad (18)$$

where all the matrices involved are frequency-independent.

4. The Padé reconstruction method

Several acceleration techniques are available. The simplest method based on Padé approximants can be improved by using a multipoint matching method [24] or the Galerkin Asymptotic Waveform Evaluation [25–27]. Here, we shall only focus on the basic Padé approximants method, also known as the Asymptotic Waveform Evaluation [27] (AWE). The frequency response computation of the mechanical system described in Eq. (16) is accelerated with the Padé approximants. This technique has already been used by the authors in a previous paper [20] for viscoelastic materials. It is briefly presented here and applied to poroelastic materials with frequency-dependent properties. Instead of solving Eq. (16) at each frequency, the solution is approximated around several central frequencies where the direct calculation is performed. The classical power series expansion

$$U_d(\omega_0 + \Delta\omega) = \sum_{i=0}^{\infty} u_i \Delta\omega^i, \quad \text{with } u_i = \frac{U_d^{(i)}(\omega_0)}{i!}, \quad (19)$$

of the solution U_d at a dof d around ω_0 is enhanced in the Padé approximant method by using a rational fraction [28Chapter 2]

$$U_d(\omega_0 + \Delta\omega) = \frac{p_0 + p_1 \Delta\omega + \dots + p_L (\Delta\omega)^L}{1 + q_1 \Delta\omega + \dots + q_M (\Delta\omega)^M} + O(\Delta\omega^{L+M+1}). \quad (20)$$

This rational function is built to agree with the $L + M + 1$ first terms of the U_d power series expansion at ω_0 but is better adapted than classical power series expansions to approximate the solution, in particular solutions with poles. The method for computing coefficients p_i and q_i is shown in Appendix B. To get these coefficients, the solution U_d and its derivatives $U_d^{(r)}$ are necessary at each central frequency ω_0 and are obtained by differentiating Eq. (17) at ω_0 according to Leibnitz's rule for the derivative of a product:

$$\begin{aligned} \mathbf{Z}_0 \mathbf{U}_0^{(k)} &= \mathbf{F}_0^{(k)} - \sum_{r=0}^{k-1} \frac{k!}{r!(k-r)!} \mathbf{Z}_0^{(k-r)} \mathbf{U}_0^{(r)}, \\ k &= 0, 1, 2, \dots, L + M + 1. \end{aligned} \quad (21)$$

Here the subscript '0' signifies that functions are evaluated at $\omega = \omega_0$. The derivatives of U_d can be obtained from Eq. (21) by a simple iterative process which requires the derivatives of \mathbf{Z}_0 and \mathbf{F}_0 . This operation is carried out using the expression of Eq. (18). The derivatives are computed analytically after realizing that all the frequency-dependent parameters are functions of the quantity: $\sqrt{1 + jC\omega}/\omega$ where the constant C can be easily identified from Eqs. (A.4) and (A.5).

Finally, from a computational point of view, a LU factorization [29,30] of the matrix \mathbf{Z}_0 is used to get \mathbf{U}_0 and its derivatives with a reordering algorithm AMD [31] to reduce the fill-in of the matrices \mathbf{L} and \mathbf{U} . Multiple RHS can be easily solved once the factorization is achieved. It is also important to note that the assembly of FE matrices is only performed once.

In our calculations, the polynomials used for the Padé approximation are taken with the same order (i.e. $M = L$), and only two parameters are adjusted to improve the quality of the reconstruction: the number of central frequencies points where the solution is expanded and the number of derivatives to get the polynomial coefficients. In practice, it is recommended to take at least one central frequency for each resonance in the studied frequency band, and to take a number of derivatives between 5 and 10.

5. Results and validations

The ZPST poroelastic model associated with the Padé approximant method is applied here on two cases: (i) a sandwich plate and (ii) a curved laminated shell. Standard 3D FE results (with quadratic shape functions) are also used as reference solutions for these two cases. The materials used in the following examples

Table 1
Characteristics of each material.

Parameters	Steel	Foam B
$E(\text{Pa})$	$2.1 \cdot 10^{11}$	$8.45 \cdot 10^5$
η_s	0.01	0.10
ν	0.3	0.3
$\rho_1(\text{kg m}^{-3})$	7800	31.16
ϕ		0.96
α_∞		1.7
$\sigma(10^3 \text{N m}^{-4} \text{s})$		32
$\Lambda(\mu\text{m})$		90
$\Lambda'(\mu\text{m})$		165

are presented in Table 1. The characteristics of the Foam B are taken from Ref. [9]. Quadratic quadrangles Q8 are used in the ZPST model, while quadratic hexahedron H20 are used in the 3D model. The same order of interpolation $p = 4$ is chosen for the displacement and pressure approximations over the thickness. Indeed, it was observed that a cubic approximation ($p = 3$) is not sufficient to get accurate results above 100 Hz. The FRFs are approximated at 10 central frequencies between 0 and 500 Hz, with 8 derivatives in the Padé reconstruction method. Finally, the mesh size is chosen as to ensure that the results have converged on the studied frequency band.

5.1. Sandwich plate

A sandwich plate of dimensions 0.2 m by 0.3 m with free boundary conditions is considered here. The skins are two identical plates of Steel and have a thickness of 1 mm. The viscoelastic core is made of Foam B and has a thickness of 2 cm. The FRF are measured at the points $M_1(0.05 \text{ m}; 0.05 \text{ m})$, $M_2(0.1 \text{ m}; 0.15 \text{ m})$, and $M_3(0.15 \text{ m}; 0.25 \text{ m})$ with an excitation placed at M_1 . The shell mesh presented in Fig. 3 is made of 12 by 18 elements (21,275 dofs), while the 3D mesh is made of 12 by 18 by 6 elements (28,122 dofs).

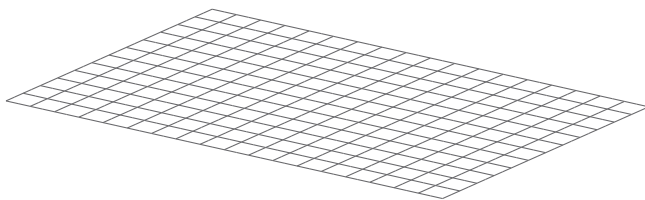


Fig. 3. Mesh used for the sandwich plate.

A FRF comparison between the ZPST model and the 3D model is presented in Fig. 4. The results obtained with the poroelastic ZPST shell element are very accurate and compare well with the standard 3D quadratic model. In addition, the computation time is also substantially reduced with the Padé approximants method. Moreover, two resonant modes are observed between the two central frequencies 225 Hz and 275 Hz and the Padé approximant method maintains a good accuracy. This clearly shows the efficiency of the reconstruction method.

An example of CPU time is presented in Table 2 for 21,275 and 37,191 dofs. One central frequency is taken into account with 25 intermediate frequencies. The solution is reconstructed over 1 element with 207 dofs. Finally, the ratio of the CPU time between the direct method and the Padé approximation method gives a speed up around 5, but the smaller is the number of dofs to reconstruct, the faster is the computation. This explains also why a speed up around 12 was found with 120 dofs to reconstruct in Ref. [20].

A convergence study of the Padé approximation is shown in Fig. 5. The convergence depends on the number of central frequencies and the number of derivatives. In the present case, five points are used to reconstruct the FRF between 0 and 250 Hz. With four derivatives, the trend is well recovered locally but discrepancies (i.e. the curve is discontinuous) are visible at the junction between frequency bands. To get better results, it is possible either to add a central frequency point near the discontinuity or to compute higher-order derivatives. In all cases, it is reasonable to limit the number of derivatives around 8 to 10.

Table 2

Example of computational times with 1 central frequency f_0 and 25 intermediate frequencies f_i taken into account. Results are observed on 1 element with 207 dofs. Calculations are made with Matlab on an Intel Xeon (R) CPU X5650, $12 \times 2.67 \text{ GHz}$, 24Go RAM, 64 bits.

	CPU time (s)			Speed up
	f_0	f_i	1 f_0 , 25 f_i	
<i>21275 dofs</i>				
Direct method	12.3	12.3	320	
Padé with 8 derivatives	12.3	23.4	57.3	5.6
Padé with 10 derivatives	12.3	30.2	69.4	4.6
Padé with 12 derivatives	12.3	36.1	78.4	4
<i>37191 dofs</i>				
Direct method	24.2	24.2	629	
Padé with 8 derivatives	24.2	39.7	102.3	6.1
Padé with 10 derivatives	24.2	51.6	123.8	5.1
Padé with 12 derivatives	24.2	65	144.4	4.4

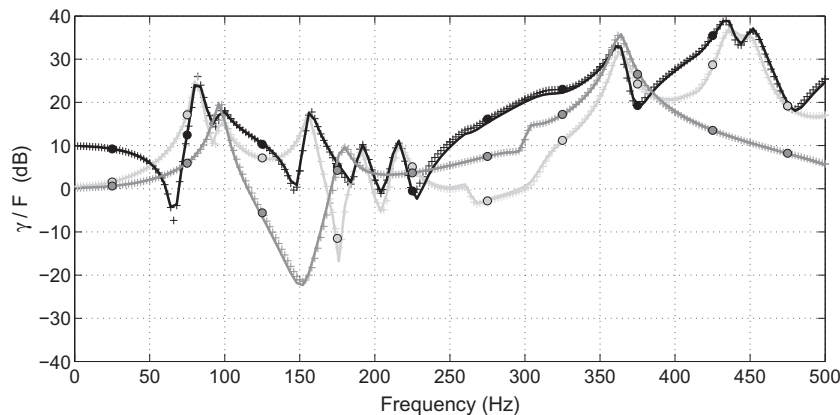


Fig. 4. FRFs comparison for the sandwich plate – Lines: 3D model – Markers +: ZPST model with an interpolation order $p = 4$ and 8 derivatives in the Padé reconstruction method – Markers o: Padé central frequencies – ■ γ_1/F_1 ■ γ_2/F_1 ■ γ_3/F_1 .

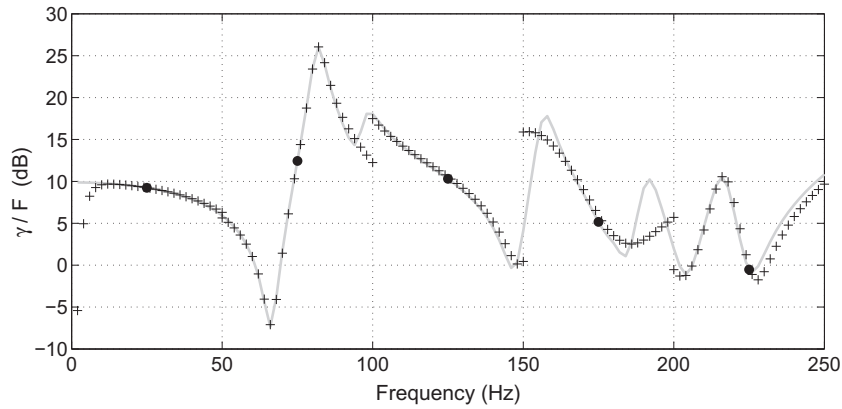


Fig. 5. Convergence of the Padé approximation for the sandwich plate – Line: reference curve with 8 derivatives – Markers +: approximation with 4 derivatives – Markers o: Padé central frequencies.

The solid displacements and the pressure distribution in the thickness at 450 Hz are shown in Fig. 6. For the sake of illustration, it is instructive to separate the different contributions stemming from the polynomial and the zigzag functions. In this example, the role of the zigzag function is essential and clearly shown.

The deformed shapes at 450 Hz of the upper skin obtained with the shell mesh and the 3D mesh are plotted in Fig. 7 (the point force is represented as the red arrow). As expected, the two models show perfect agreement. The well known mass-spring-mass frequency estimated around 630 Hz can also be identified when dealing with a normal plane wave excitation (i.e. the force is uniformly distributed on the upper skin). The opposition of phase between the two skins can be observed in this case and this is shown in Fig. 8.

In acoustics, this particular frequency highly deteriorates the sound insulation properties of a multilayered panel compared to an equivalent homogeneous panel. However the sound insulation of the multilayered panel increases also highly above this mass-spring-mass frequency. To illustrate these phenomenon,

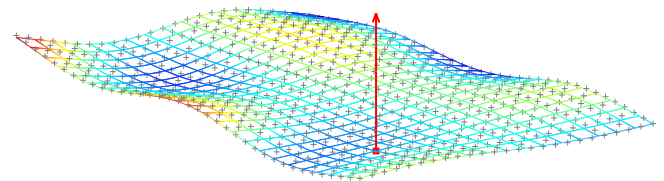


Fig. 7. Deformed shape of the upper skin – Lines: ZPST model – Markers +: 3D model.

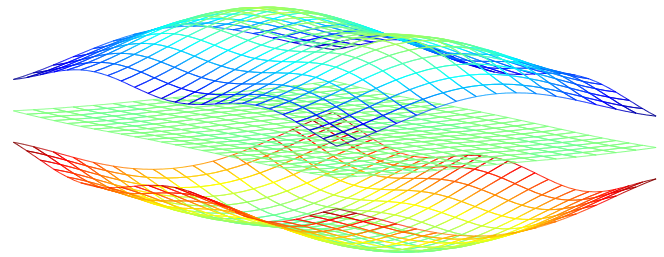


Fig. 8. Deformed shape of the sandwich plate at the mass-spring-mass resonance frequency 630 Hz.

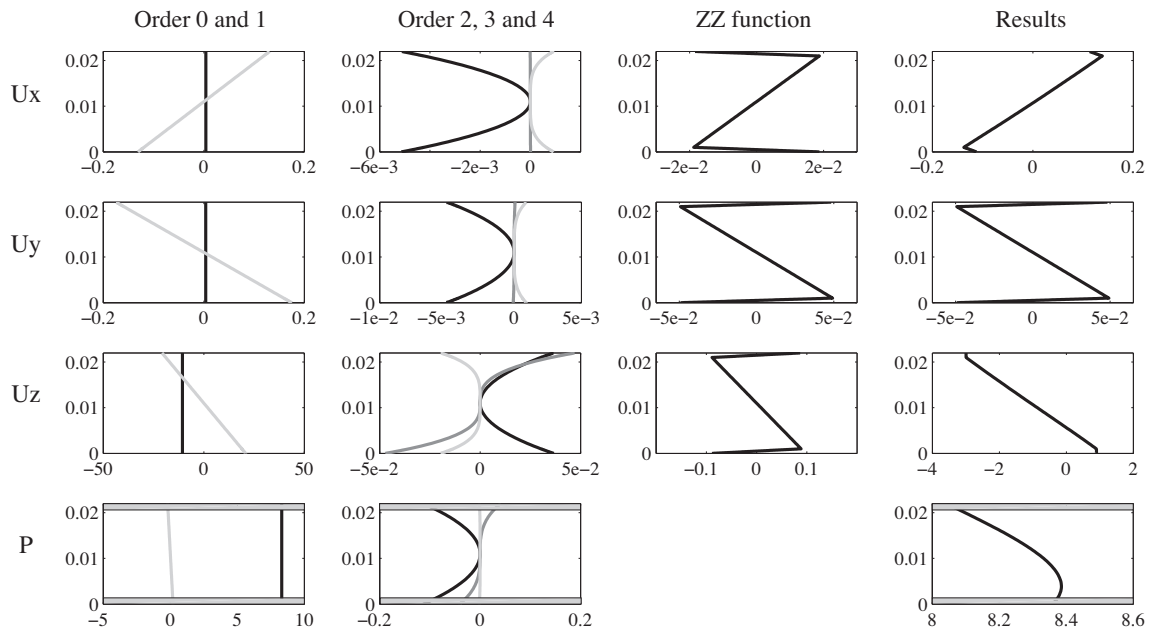


Fig. 6. Solid displacements (μm) and pressure (Pa) distribution in the thickness at M_1 with the ZPST model at 450 Hz.

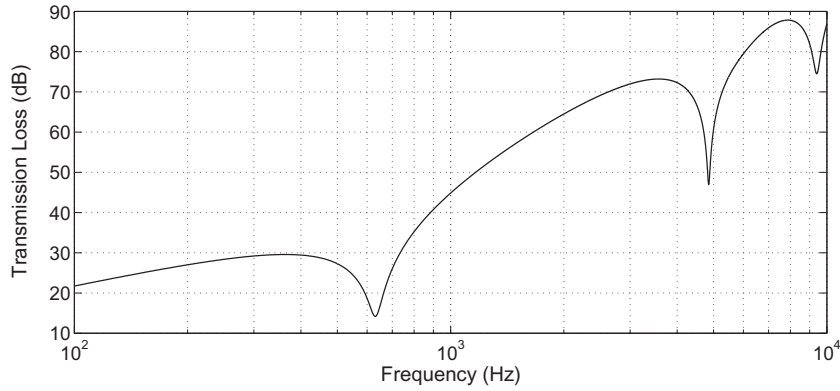


Fig. 9. Transmission loss of the sandwich plate calculated with the Transfer Matrix Method.

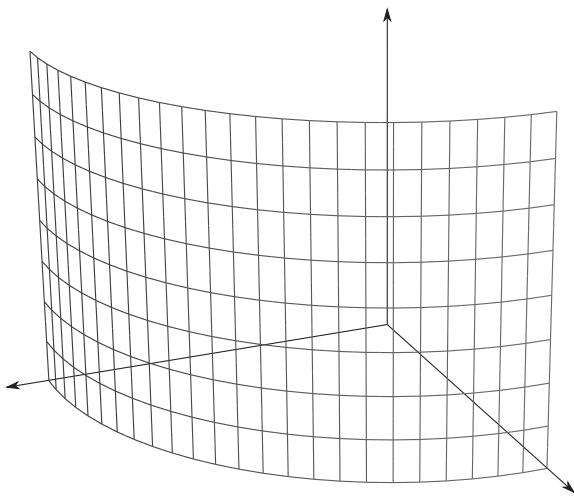


Fig. 10. 2D mesh used for the curved laminated shell.

the transmission loss of a similar infinite sandwich panel submitted to a normal plane wave calculated with a Transfer Matrix Method [32] is presented in Fig. 9. The coincidence frequency is visible at high frequency, while the mass-spring-mass resonance frequency leads to a dip in the transmission loss curve at 630 Hz.

5.2. Curved laminated shell

In this section, the poroelastic shell element is compared with a 3D finite element on a curved geometry. The tested multilayered sample is a quarter of a cylinder with two layers of dimensions $R = 0.2$ m and $H = 0.2$ m. This shape was chosen in order to demonstrate the validity of the ZPST porous model for tackling curved geometries that are often encountered in aeronautics, aerospace, and rail industry. The interior layer is made of Steel and has a thickness of 1 mm. The poroelastic upper layer is made of Foam B and has a thickness of 3 cm. Three points are considered to identify input and transfer mobilities: $M_1(\theta = \pi/8; H = 0.025$ m), $M_2(\theta = 3\pi/8; H = 0.175$ m), and $M_3(\theta = \pi/8; H = 0.175$ m) with an excitation placed at M_1 . Free boundary conditions are applied in both models. The 2D mesh presented in Fig. 10 is made of 24 by 8 elements (19,159 dofs), while the 3D mesh is made of 3 by 32 by 16 elements (35,565 dofs). Here, it is worth noticing that the gain in dofs is more important for thicker panels.

The coupling with the fluid domain is not considered in this paper. An impervious condition at the interface with the infinite acoustic domain is applied. In this case, the total stress of the poroelastic layer is null at the interface, and there is no relative mass flux through the interface.

Input and transfer mobilities for the curved shell are compared with the two models in Fig. 11. The results obtained with the poroelastic ZPST model are in good agreement with the 3D model over the whole frequency band. The accuracy of the Padé approximation method is also demonstrated here. However,

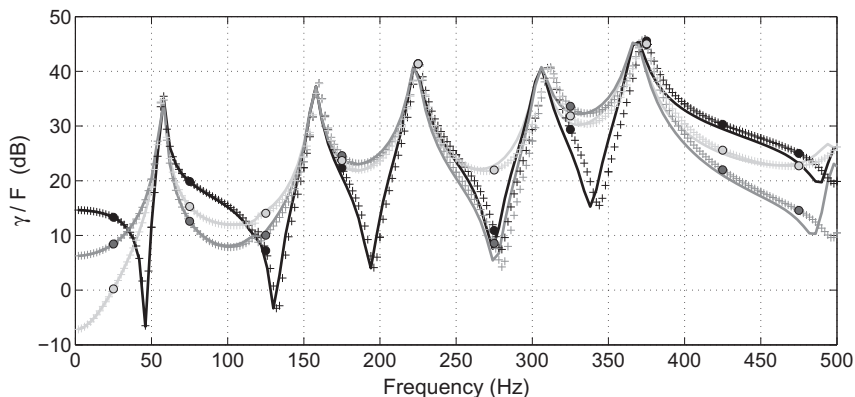


Fig. 11. FRFs comparison for the curved laminated shell – Lines: 3D model – Markers +: ZPST model with an interpolation order $p = 4$ and 8 derivatives in the Padé reconstruction method – Markers \circ : Padé central frequencies – \blacksquare γ_1/F_1 \blacksquare γ_2/F_1 \blacksquare γ_3/F_1 .

the number of central frequencies and the number of derivatives must still be chosen carefully to obtain the convergence of the Padé approximation.

6. Conclusions and prospects

The efficiency of the ZPST shell element for the wave propagation modeling through curved multilayered structures with poroelastic materials has been demonstrated in this paper. The model offers two main advantages: (i) it reduces the time spent on mesh preparation and (ii) it significantly reduces the computational effort while maintaining a good level of accuracy comparable with conventional 3D models. Frequency dependent material properties have been taken into account for the poroelastic layers. The Padé approximant method has also been applied successfully in order to speed up the numerical evaluation of the FRFs.

Acknowledgments

The authors acknowledge the project MAEVA and their industrial partners in this project: ESI Group, Vibratex, and Arcelor-Mittal. The authors acknowledge also the Project Pluri-Formations PILCAM2 at the Université de Technologie de Compiègne for providing HPC resources that have contributed to the research results reported within [33].

Appendix A. Porous model

A.1. Inertial coupling coefficients

The inertial coefficients ρ_{11} , ρ_{22} , ρ_{12} are related to the densities ρ_s of the skeleton, ρ_f of the fluid phase, and ρ_0 of the air such as:

$$\rho_{11} = \rho_s + \phi\rho_f - \phi\rho_0, \quad (\text{A.1})$$

$$\rho_{12} = -\phi\rho_f + \phi\rho_0, \quad (\text{A.2})$$

$$\rho_{22} = \phi\rho_f. \quad (\text{A.3})$$

Viscous and thermal dissipations are taken into account by the frequency-dependent Johnson–Allard's expressions of the fluid density ρ_f and the dynamic fluid compressibility K_f :

$$\rho_f = \rho_0\alpha_\infty \left(1 - \frac{\sigma\phi}{j\rho_0\alpha_\infty\omega} \sqrt{1 - 4j \frac{\eta\alpha_\infty^2\omega\rho_0}{\Lambda^2\phi^2\sigma^2}} \right), \quad (\text{A.4})$$

$$K_f = \frac{\gamma P_0}{\gamma - (\gamma - 1) \left(1 - \frac{8\eta\sqrt{1 - j\rho_0\frac{\text{Pr}\Lambda^2\omega}{16\eta}}}{j\Lambda^2\text{Pr}\omega\rho_0} \right)^{-1}}, \quad (\text{A.5})$$

respectively, with $j^2 = -1$. These expressions are given with a time dependence in $e^{-j\omega t}$ and involve five parameters: the porosity ϕ , the tortuosity α_∞ , the airflow resistivity σ , and the viscous and thermal characteristic lengths Λ and Λ' . The surrounding air is also described by the static pressure P_0 , the dynamic viscosity η and the Prandtl number Pr .

A.2. Elastic coefficients

The simplified elastic coefficients A , Q , and R used in Biot's model are given by:

$$A = \frac{4}{3}N + K_b + \frac{(1 - \phi)^2}{\phi}K_f, \quad (\text{A.6})$$

$$Q = \frac{R(1 - \phi)}{\phi}, \quad (\text{A.7})$$

$$R = \phi K_f, \quad (\text{A.8})$$

where N is the shear modulus, K_b is the bulk modulus of the solid frame, ϕ is the porosity, and K_f is the fluid compressibility modulus.

Appendix B. Padé coefficients calculation

The polynomials P and Q have to be computed for each dof $d \in \mathcal{D}$ and for each value of $\omega_0 \in \Omega$. To obtain the coefficients p_i and q_i , Eq. (20) is rewritten as

$$U_d(\omega_0 + \Delta\omega)Q(\Delta\omega) = P(\Delta\omega) + O(\Delta\omega^{M+L+1}). \quad (\text{B.1})$$

Applying Liebnitz's rule on the derivative of a product [343.3.8] with respect to $\Delta\omega$ yields [28, Chapter 2]

$$\begin{pmatrix} u_{L-M+1} & u_{L-M+2} & \dots & u_L \\ u_{L-M+2} & u_{L-M+3} & \dots & u_{L+1} \\ \vdots & \vdots & & \vdots \\ u_L & u_{L+1} & \dots & u_{L+M+1} \end{pmatrix} \begin{pmatrix} q_M \\ q_{M-1} \\ \vdots \\ q_1 \end{pmatrix} = \begin{pmatrix} u_{L+1} \\ u_{L+2} \\ \vdots \\ u_{L+M} \end{pmatrix}, \quad (\text{B.2})$$

and

$$p_i = \sum_{k=0}^i q_k u_{k-i}, \quad (\text{B.3})$$

with $u_i = 0$ if $i < 0$ by convention. The denominator coefficients q_i are found by solving Eq. (B.2). Note this matrix is Toeplitz [28, Chapter 2] (or Hankel according the order of the unknowns) and can be inverted in $O(n^2)$ operations instead of $O(n^3)$ for arbitrary systems (n is the matrix size). Nonetheless, a standard inversion is used in this paper. Even if the condition number is high, the computation of the coefficients q_i remains robust. Once this is done, the numerators coefficients p_i are deduced from the q_i 's using Eq. (B.3). As u_i appears in Eqs. (B.3) and (B.2), it is required to compute the power expansion of U_d as a prior condition by using the derivatives of U_d at ω_0 :

$$u_i = \frac{U_d^{(i)}(\omega_0)}{i!}. \quad (\text{B.4})$$

References

- [1] Atalla N, Panneton R, Debergue P. A mixed displacement–pressure formulation for poroelastic materials. *J Acoust Soc Am* 1998;104(3):1444–52.
- [2] Atalla N, Hamdi MA, Panneton R. Enhanced weak integral formulation for the mixed (u,p) poroelastic equations. *J Acoust Soc Am* 2001;109(6):3065–8.
- [3] Biot M. Theory of propagation of elastic waves in a fluid-saturated porous solid. I: Low-frequency range. *J Acoust Soc Am* 1956;28(2):168–78.
- [4] Biot M. Theory of propagation of elastic waves in a fluid-saturated porous solid. II: Higher frequency range. *J Acoust Soc Am* 1956;28(2):179–91.
- [5] Biot M. Generalized theory of acoustic propagation in porous dissipative media. *J Acoust Soc Am* 1962;34(9):168–78.
- [6] Ouisse M, Ichchou M, Chedly S, Collet M. On the sensitivity analysis of porous material models. *J Sound Vib* 2012;331(24):5292–308.
- [7] Doutres O, Dauchez N, Gènevaux J, Dazel O. Validity of the limp model for porous materials: a criterion based on the Biot theory. *J Acoust Soc Am* 2007;122(4):2038–48.
- [8] Chazot J, Guyader J. Acoustic modeling of light and non-cohesive poro-granular materials with a fluid/fluid model. *Acta Mech*. 2008;195(1–4):227–47.
- [9] Jaouen L, Brouard B, Atalla N, Langlois C. A simplified numerical model for a plate backed by a thin foam layer in the low frequency range. *J Acoust Soc Am* 2005;280:681–98.
- [10] Kärger L, Wetzel A, Rolfes R, Rohwer K. A three-layered sandwich element with improved transverse shear stiffness and stresses based on FSDT. *Comput Struct* 2006;84(13–14):843–54.
- [11] Amichi K, Atalla N. A new 3D finite element for sandwich beams with a viscoelastic core. *J Vib Acoust* 2009;131(2):1–9.
- [12] Cugnoni J, Gmür T, Schorderet A. Modal validation of a set of C0-compatible composite shell finite elements. *Compos Sci Technol* 2004;64(13–14):2039–50.

- [13] Cugnoni J, Gmür T, Schorderet A. Identification by modal analysis of composite structures modelled with FSDT and HSDT laminated shell finite elements. *Compos Part A: Appl Sci Manuf* 2004;35(7–8):977–87.
- [14] Matter M, Gmür T, Cugnoni J, Schorderet A. A PSDT shell finite element formulation including structural damping. *Comput Struct* 2010;88(15–16):902–8.
- [15] Murakami H. Laminated composite plate theory with improved in-plane response. *J Appl Mech* 1986;53(3):661–7.
- [16] Carrera E. Historical review of zig-zag theories for multilayered plates and shells. *Appl Mech Rev* 2003;56(3):287–308.
- [17] Carrera E. On the use of the Murakami's zig-zag function in the modeling of layered plates and shells. *Comput Struct* 2004;82:541–54.
- [18] Sulmonì M, Gmür T, Cugnoni J, Matter M. Modal validation of sandwich shell finite elements based on a p -order shear deformation theory including zigzag terms. *Int J Numer Methods Eng* 2008;75:1301–19.
- [19] Fares M, Elmarghany M. A refined zigzag nonlinear first-order shear deformation theory of composite laminated plates. *Compos Struct* 2008;82(1):71–83.
- [20] Chazot J, Nennig B, Chettah A. Harmonic response computation of viscoelastic multilayered structures using a ZPST shell element. *Comput Struct* 2011;85(23–24):2522–30.
- [21] Dazel O, Sgard F, Lamarque C, Atalla N. An extension of complex modes for the resolution of finite-element poroelastic problems. *J Sound Vib* 2002;253(2):421–45.
- [22] Rumpler R, Legay A, Deü J-F. Performance of a restrained-interface substructuring FE model for reduction of structural-acoustic problems with poroelastic damping. *Comput Struct* 2011;89(23–24):2233–48.
- [23] Rumpler R, Deü J, Göransson P. A modal-based reduction method for sound absorbing porous materials in poro-acoustic finite element models. *J Acoust Soc Am* 2012;132(5):3162–79.
- [24] Avery P, Farhat C, Reese G. Fast frequency sweep computations using a multi-point Padé-based reconstruction method and an efficient iterative solver. *Int J Numer Methods Eng* 2007;69(13):2848–75.
- [25] Slone R, Lee J, Lee R. Automating multipoint Galerkin awe for a FEM fast frequency sweep. *Electromagnetics* 2002;22(4):275–89.
- [26] Hetmaniuk U, Tezaur R, Farhat C. Review and assessment of interpolatory model order reduction methods for frequency response structural dynamics and acoustics problems. *Int J Numer Methods Eng* 2012;90(13):1636–62.
- [27] Slone R, Lee J, Lee R. Automating multipoint Galerkin awe for a FEM fast frequency sweep. *IEEE Trans. Magnet.* 2002;38(2):637–40.
- [28] P.R. Graves-Morris, G.A.J. Baker, Padé Approximants, *Encyclopedia of Mathematics*, Addison-Wesley (ed.), Cambridge University Press, 1981.
- [29] Davis TA. Algorithm 832: Umfpack an unsymmetric-pattern multifrontal method. *ACM Trans. Math. Softw.* 2004;30(2):196–9.
- [30] Amestoy PR, Duff IS, L'Excellent J-Y. Multifrontal parallel distributed symmetric and unsymmetric solvers. *Comput. Methods Appl. Mech. Eng.* 2000;184:501–20.
- [31] Amestoy PR, Davis TA, Duff IS. Algorithm 837: AMD, an approximate minimum degree ordering algorithm. *ACM Trans. Math. Softw.* 2004;30(3):381–8.
- [32] Brouard B, Lafarge D, Allard J. A general method of modeling sound propagation in layered media. *J Sound Vib* 1995;183(1):129–42.
- [33] <<http://pilcam2.wikispaces.com>>.
- [34] Abramowitz A, Stegun I. *Handbook of mathematical functions*. New York: Dover Publ.; 1965.